Available online at www.sciencedirect.com

jmr&t Journal of Materials Research and Technology

journal homepage: www.elsevier.com/locate/jmrt

Original Article

Effect of yttrium addition on phase transformations in alloy 718

Rosa Maria Sales da Silveira [a,*], Alessandra Vieira Guimarães [a], Clarissa Hadad de Melo [b,c], Rafaella Martins Ribeiro [a], Alexandre Bellegard Farina [d], Loïc Malet [e], Luiz Henrique de Almeida [a], Leonardo Sales Araujo [a]

[a] Programa de Engenharia Metalúrgica e de Materiais, Universidade Federal do Rio de Janeiro, Brazil
[b] DEMM, Department of Metallurgical and Materials Engineering, University of Porto, Portugal
[c] LAETA/INEGI—Institute of Science and Innovation in Mechanical and Industrial Engineering, Porto, Portugal
[d] Research and Development Center, Villares Metals S.A, Brazil
[e] 4Mat, Université Libre de Bruxelles, Belgium

ARTICLE INFO

Article history:
Received 23 January 2022
Accepted 24 March 2022
Available online 3 April 2022

Keywords:
Alloy 718
Yttrium addition
Thermodynamic calculations
Differential scanning calorimetry

ABSTRACT

The nickel-base alloy 718 is widely used due to its superior performance at high temperatures, combining properties such as high strength, high corrosion and oxidation resistances and good formability and weldability. Its properties can be further improved by controlled additions of alloying elements such as Ce, W, Mo, P, B and Y. The present work aims to evaluate the effect of the yttrium alloying on the phase transformation in alloy 718. Thermodynamic calculation, scanning electron microscopy, electron backscattered diffraction, hardness measurements and differential scanning calorimetry tests were conducted. The $Ni_{17}Y_2$ phase was observed in two situations: associated with the Nb-rich particles or as single particles. The addition of yttrium has a remarkable effect on grain size control. The differential scanning calorimetry tests indicated that the alloy with the high Y content showed earlier precipitation of the γ" phase (Ni_3Nb), which is the main hardening contributor, resulting in an increase in hardness.

1. Introduction

The nickel-base alloy 718 is widely used due to its superior performance at high temperatures (up to 650 °C), with improved properties such as high strength, high corrosion and oxidation resistances, good formability and weldability [1]. The alloy presents a complex metallurgy [2]: Cr is a solid solution hardener and improves corrosion and oxidation resistance; Al improves oxidation resistance and, along with Ti, induces the formation of the hardening precipitate γ' (Ni3(Al,Ti), FCC, coherent, $L1_2$). Ti and Nb are carbidonitride formers. Mo is a solid solution hardener and improves creep

* Corresponding author.
E-mail address: rosasilveira@metalmat.ufrj.br (R.M.S. Silveira).
https://doi.org/10.1016/j.jmrt.2022.03.137

resistance. Fe, in addition to the solid solution hardening, lowers the alloying cost. Regarding Nb, compared to the other precipitation hardened nickel-based superalloys, its content can reach up to 5.5 wt.%, resulting in solid solution hardening and the precipitation of the metastable, ordered and coherent, BCT γ" phase ($Ni_3Nb - D0_{22}$), which is the major contributor to the high-temperature strength [2].

The MC carbonitrides - mainly (Nb,Ti) (C,N) - are also present in the microstructure and stable up to 1200 °C [2]. During long-term aging operations at temperatures above 700 °C, the metastable γ" phase starts to be dissolved and gives way to the orthorhombic δ phase (Ni_3Nb), which is stable and incoherent with the face-centered cubic γ matrix [3,4]. The δ particles can also be precipitated directly from the austenitic matrix, preferentially nucleating at grain boundaries as plates and/or globular morphologies and can be used to control the grain size for strength optimization [5].

Multiple studies have described improved superalloys properties by adding different elements such as Ce, W, Mo and P, among others [6–9]. Particularly, the addition of yttrium to the composition of superalloys has been studied due to its promising results on mechanical properties and high-temperature oxidation resistance [6,10–12]. Yttrium addition in superalloys presents many beneficial effects when properly added. It was reported that the Y addition increases the carbide fragmentation in nickel-based and austenitic alloys, being a positive contribution for creep resistance [13–15] and also leading to an improvement of hardness due to the solid-solution strengthening effect. Additionally, the grain size is controlled by Y contents [15,16]. The high affinity between yttrium and sulfur produces Y-rich stable sulfides that can be removed during casting, reducing the sulfur segregation on oxide/matrix interfaces and grain boundaries, which increases their cohesion and leads to higher oxidation resistance and ductility of alloy 718 [6,11,16,17].

Additionally, Y will preferentially react with oxygen during melting, forming Y_2O_3 which subsequently forms an alkaline slag favorable for desulfurization [18]. However, as for different addition elements, the beneficial effect is related to a concentration range and, particularly for Y, when in excess, generates intense precipitation of yttrium-rich phases that serve as preferential sites to crack nucleation and propagation [12]. Few studies have addressed the Y addition in alloy 718. Most of the studies about yttrium additions in nickel alloys focus on evaluating either corrosion or mechanical properties, mainly for cast conditions [12,19–28]. Also, Y is usually added as Y_2O_3 by powder metallurgy for ODS Ni-base superalloys to increase oxidation resistance and mechanical performance [29–32]. A previous work [15] analyzed the alloy 718 with 0.05 and 0.61 wt.% Y on solubilized conditions with no δ phase precipitates. These authors reported the formation of different Y-rich phases, such as Y sulphides and oxides, and the $Ni_{17}Y_2$ phase; this latter, with its volume fraction increasing with the Y content. A high proportion of this phase was deleterious to the mechanical properties of the alloy, causing a sharp decrease in ductility. However, a controlled Y content increased (by around 20%) the alloy's ductility at room temperature.

Aiming to evaluate the effect of the yttrium alloying on the phase transformations in alloy 718, thermodynamic calculations, scanning electron microscopy and electron backscattered diffraction, hardness measurements and differential scanning calorimetry tests were conducted.

Thermodynamic calculations showed the Y effect on decreasing liquidus temperature of alloy 718. Our data are consistent with the influence of Y on δ phase precipitation as a consequence of Y-rich phases precipitation and its cleaning effect on grain boundaries. A high Y content contributed to γ″ precipitation, resulting in increased strength.

2. Materials and methods

Three alloys were cast in a vacuum induction furnace. One, acting as a reference, was melted with no Y addition. The other two alloys were melted with nominal wt.% Y additions of 0.1% Y and 1.0%. To maximize the Y yield into the alloy during melting, this element was added close to the end of the melting, 5 min before pouring the metal into the casting. The Y yield calculation is discussed elsewhere [15].

Table 1 shows the chemical composition of the alloys, referred to as alloys A, B and C. The Y content was determined by wet chemical analysis. C, N, O and S were obtained by the combustion method and the remaining elements by optical emission spectroscopy, with the latter method previously calibrated by wet chemical method.

The ingots were subsequently homogenized and then hot forged into round bars. After forging, the alloys were submitted to a solution annealing heat treatment, performed at 975 °C for 1 h, followed by quenching in water [33].

Thermodynamic calculations were performed with the Thermocalc 2018a [34], with the integration of the TCNI8 [35] and TCOX [36] databases, to estimate the stable phases formed and their mass fractions, as well as the composition profile of the liquid during solidification. The microstructures of solubilized alloys were analyzed by scanning electron microscopy (SEM) in backscattered mode, using a Tescan Vega 3, with 20 kV of acceleration voltage. The phases were identified by energy-dispersive X-ray spectrometry (EDS). The δ, $Ni_{17}Y_2$ and the (Nb,Ti) (C,N) particles were quantified using ImageJ® software, from thresholding and binarization of 8-bit backscattered electron (BSE) images through BioVoxxel_toolbox plugin. Five random fields at a nominal magnification of 2000 × were collected for each alloy.

Table 1 – Chemical composition (weight.%) of the samples.

Alloy	Ni	Cr	Fe	Mo	Nb	Al	Ti	Mn	Si	C	S	O	N	Y
A	52.7	17.81	19.71	2.90	5.10	0.518	0.972	0.04	0.07	0.026	0.0040	0.0042	0.0110	**0.00**
B	52.5	17.80	20.05	2.90	4.99	0.519	0.980	0.02	0.07	0.023	0.0016	0.0020	0.0055	**0.05**
C	51.4	17.62	20.69	2.91	5.01	0.549	0.966	0.03	0.08	0.024	0.0010	0.0012	0.0060	**0.61**

To identify the Y-rich phase, an electron backscattered diffraction (EBSD) analysis was performed on B and C samples. Optical microscopy (OM), model AxioCam MRc 5, was used to measure the grain size. The Heyn method was used based on ASTM E112 [37]. Sample preparation consisted of grinding with sandpaper up to 1200 mesh, followed by polishing with diamond paste with 6, 3 and 1 μm. Differential scanning calorimetry (DSC) was performed on a TGA & DTA/DSC thermal analyzer SETARAM from room temperature to 1100 °C using a heating rate of 10 °C/min. Samples of solubilized alloys were cut and mechanically polished to remove any possible contaminated surface layer. Afterward, they were cleaned with 99% ethanol and placed in an alumina crucible. The measurements were carried out under a flowing argon atmosphere. All obtained DSC curves were normalized for the initial sample mass. A deconvolution process was done to define the onset, peak and end temperatures for each peak identified on DSC records.

To evaluate the differences in mechanical properties due to the precipitation of the hardening phases, for each sample, the Rockwell C hardness of the aged samples was measured, with five indentations per sample. The aging heat treatment of the samples was 800 °C for 6 h.

3. Results and discussion

3.1. *Thermodynamic calculations*

Figure 1 shows a step cooling diagram for the formation of the main second phases for alloys B and C. From the liquid, initially, the phase Ni_3Y is formed and its stability range is between 1050 and 1100 °C. During solidification, there is strong segregation of Nb and Y into the interdendritic liquid, as shown in Fig. 2 for alloys B and C, which will lower the liquidus temperature and favor the precipitation of the Y-rich phase Ni_3Y and the Nb-rich phases, like Laves, (Nb,Ti)C and δ.

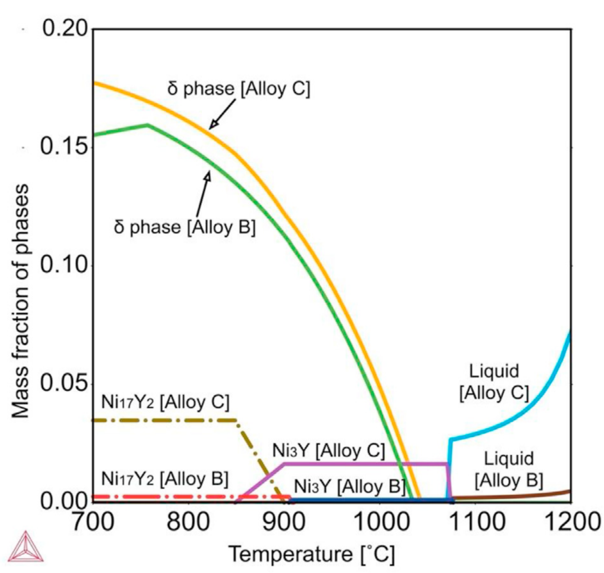

Fig. 1 – Thermodynamic calculations of the stable phases formed along the temperature range for alloys B and C.

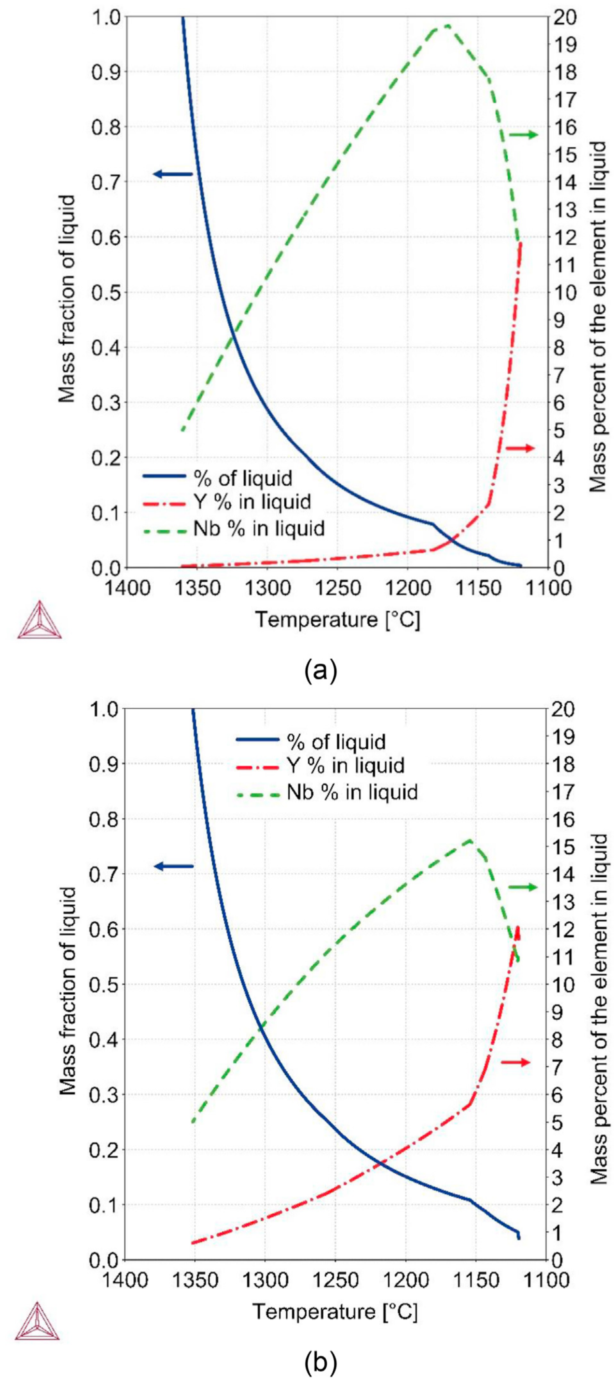

Fig. 2 – Calculation of the segregation of Y and Nb into the liquid versus mass fraction of the liquid for: (a) alloy B; (b) alloy C.

The segregation into the liquid during solidification can rise to ~12 wt.% Y and ~20 wt.% Nb for alloy B, compared to ~12 wt.% Y and ~15 wt.% Nb for alloy C. Regarding the Nb content, the drop in the segregation level in the final phase of solidification is due to the formation of the Nb-rich Laves and δ and the Y-rich Ni_3Y. The Laves and δ phases can, posteriorly, be solubilized during the homogenization heat treatment, commonly applied for alloy 718. However, it is important to consider that the homogenization heat treatment for this

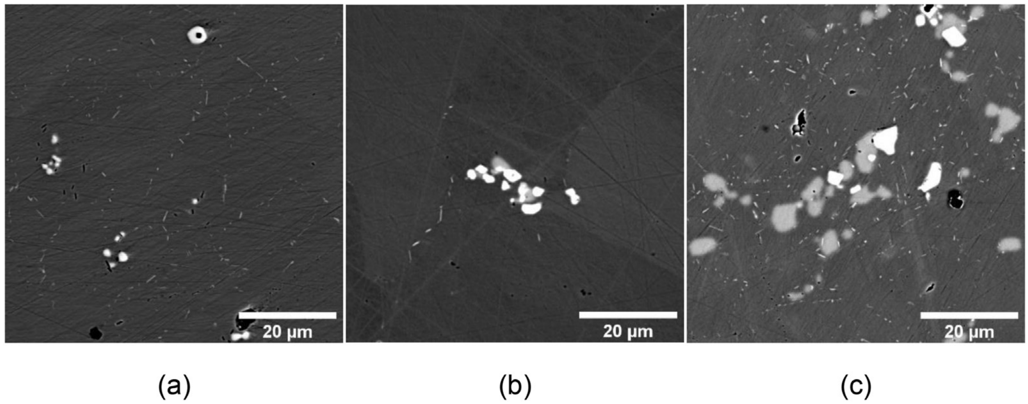

Fig. 3 – SEM images of the microstructure of alloys A (a), B (b) and C (c) (backscattered mode). For alloys B (b) and C (c), it is possible to evidence the associated precipitation of the primary (Nb, Ti) (C, N) (white particles) with the $Ni_{17}Y_2$ (bulky, light gray particles). The small, needle like particles: δ phase.

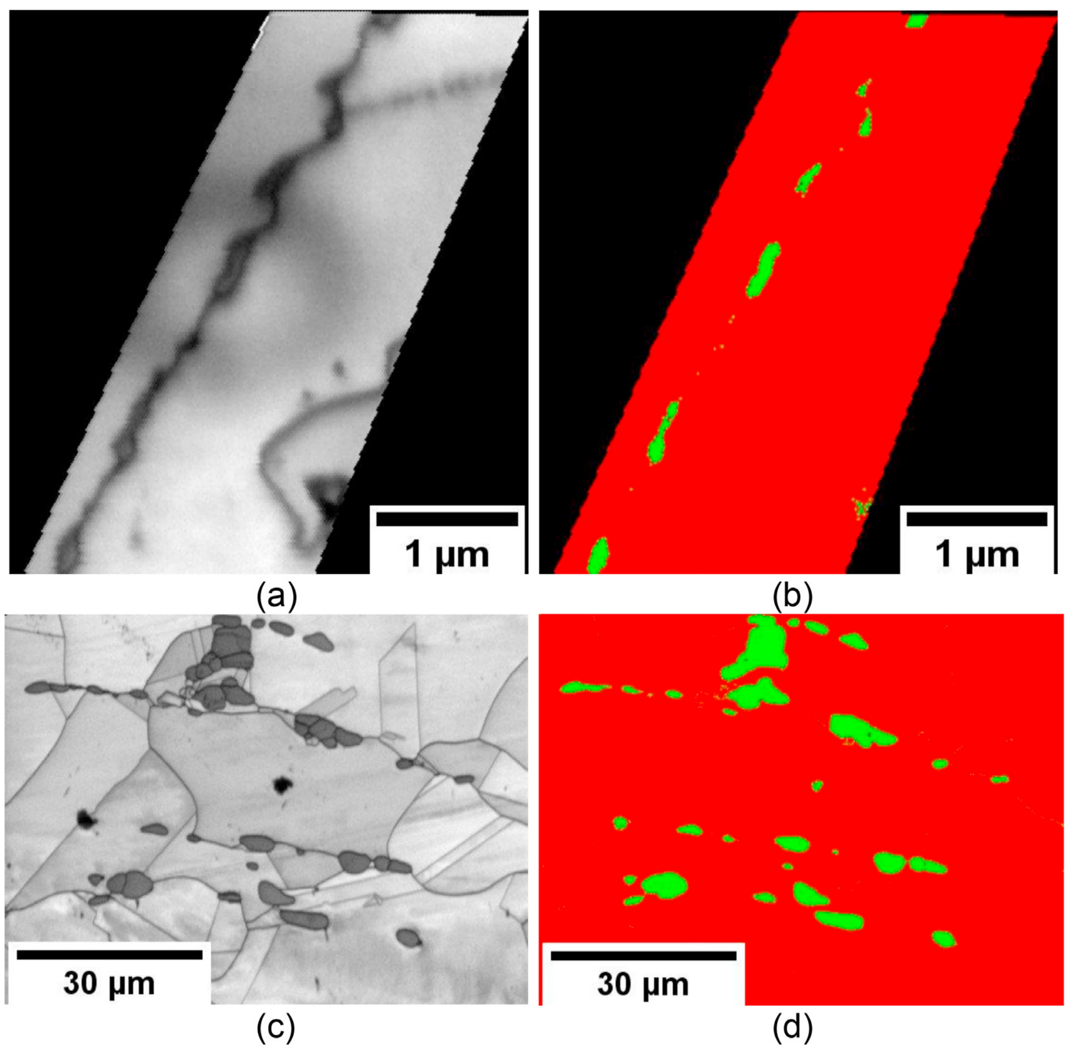

Fig. 4 – EBSD mappings of the $Ni_{17}Y_2$ particles: (a) and (c): band contrast images of the B and C samples, respectively; (b) and (d) phase maps of the B and C samples, respectively. Red: fcc matrix; Green: $Ni_{17}Y_2$.

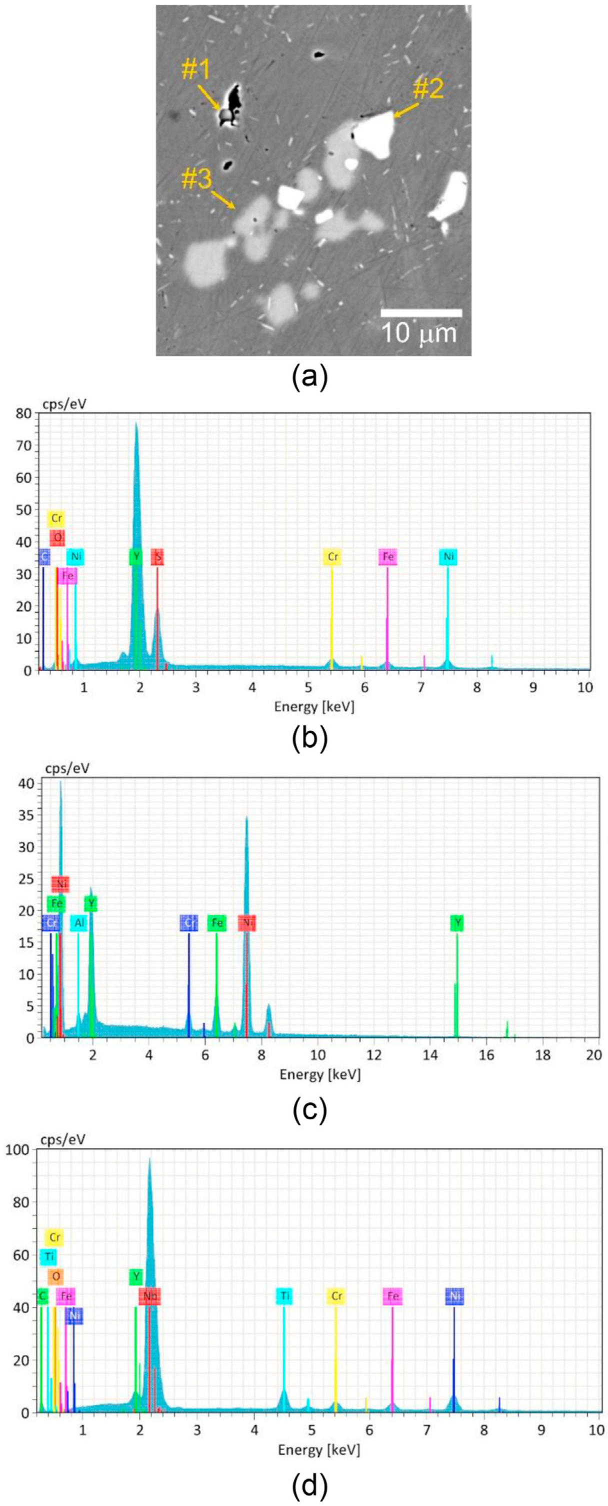

Fig. 5 – a) microstructure of sample C, showing the associated precipitation of the (Nb,Ti) (C,N) and $Ni_{17}Y_2$ particles. The small and disperse light gray particles: δ phase. The yellow arrows indicate the particles analyzed by EDS; (b) yttrium sulphides; (c) $Ni_{17}Y_2$ particle; (d) (Nb,Ti) (C,N) particle.

alloy may have to be shifted to lower temperatures to avoid localized liquation, due to the lower liquidus temperature induced by the combined effect of Nb and Y segregation. Upon cooling, the Ni_3Y is transformed to the $Ni_{17}Y_2$ phase. While, for alloy B, the transition is sharp at circa 945 °C, for alloy C, the Ni_3Y to $Ni_{17}Y_2$ transformation occurs between 930 and 880 °C. For alloy B, the predicted mass fraction of $Ni_{17}Y_2$ is less than 0.2%, while for alloy C, it is ~4.0%. Despite that the solubilization temperature was defined in the Ni_3Y range, upon cooling, there is a drive to the transformation to $Ni_{17}Y_2$.

A previous work [15] evidenced the $Ni_{17}Y_2$ phase in hot forged bars after solubilization heat treatment. Wang et al. [38], investigating 0.1 wt.% Y addition in alloy 718 produced by rapid solidification observed Ni_3Y in the as-cast strip. After homogenization, cold rolling and annealing heat treatment at 950 °C for 3 h, the authors evidenced $Ni_{17}Y_2$ particles. Cao et al. [39], analyzing the effect of Y contents up to 0.1 wt.% on purification and carbide morphology of a cast superalloy K4169 – which has a very similar composition to alloy 718 – observed $Ni_{17}Y_2$ as well. These findings sustain the assumption that the Ni_3Y phase may occur for very high cooling rates after melting, being promptly replaced by the more stable $Ni_{17}Y_2$ phase. This phase presents a hexagonal crystal structure (no related structurbericht, spacegroup: $P6_3/mmc$) [40,41].

Regarding the precipitation of the γ" and δ phases, no relevant variations were observed between all alloys for the solubility temperature: ~1040 °C for δ and ~920 °C for γ"; and mass fraction: ~6.8% for δ at 975 °C and ~7.0% for γ" at 720 °C. For the γ' phase the solubility temperatures are 780, 801 and 771 °C for alloys A, B and C, respectively, while the mass fraction at 720 °C was 2.2, 3.0 and 1.8%, respectively.

3.2. *Microstructural characterization*

The microstructures observed with backscattered mode of solubilized alloys are shown in Fig. 3. Alloy A consists of (Nb,Ti) (C,N) strings and δ particles on grain boundaries. The Y modified alloys presented the precipitation of the (Nb,Ti)C particles associated with the Y-rich particles. The Y-rich particles were previously defined by Guimarães et al. [15] as $Ni_{17}Y_2$, with a hexagonal structure and a = 0.8320 nm and c = 0.8042 nm. Fig. 4 shows the EBSD mappings of the Y-rich particles, corroborating its identification as $Ni_{17}Y_2$. On one hand, there is associated precipitation with the primary (Nb,Ti) (C,N) particles. During solidification, there is strong segregation of Nb and Y to the melt. Mattern et al. [42] reported an extensive immiscibility in the Nb-Y system, leading to the formation of Nb-rich and Y-rich regions and, consequently, Nb-rich and Y-rich phases. This was observed for alloys B and C (Fig. 3).

On the other hand, the $Ni_{17}Y_2$ was also observed as fine particles, mainly along grain boundaries for sample B and as inter and intragranular coarse particles for sample C. It is important to note that, as previously evidenced through thermodynamic calculations, the higher Y content led to a higher mass fraction of the $Ni_{17}Y_2$ phase. In addition to this phase, Y-rich sulfides were also identified by EDS (Fig. 5). Cao et al. [39] also identified sulfides and predicted the formation of Y-S, acting as a desulphurization product.

Table 2 – austenite grain size and area fraction of δ phase.

Sample	Mean grain size (μm)	Area fraction (%)		
		δ	(Nb,Ti) (C,N)	$Ni_{17}Y_2$
A	20.6 ± 1.9	0.51 ± 0.19	0.42 ± 0.32	–
B	32.9 ± 4.4	0.09 ± 0.04	0.36 ± 0.14	0.18 ± 0.10
C	14.9 ± 1.2	0.60 ± 0.20	0.32 ± 0.31	3.16 ± 0.36

Due to the δ sub-solvus solution heat treatment, the δ particles are precipitated mainly along grain boundaries, pinning grain boundaries and, therefore, preventing further grain growth. The area fraction of the $Ni_{17}Y_2$ and (Nb,Ti) (C,N) particles were close to the values calculated through the thermodynamic calculations. Table 2 presents the mean grain sizes and δ, $Ni_{17}Y_2$ and (Nb,Ti) (C,N) area fractions for A, B and C samples.

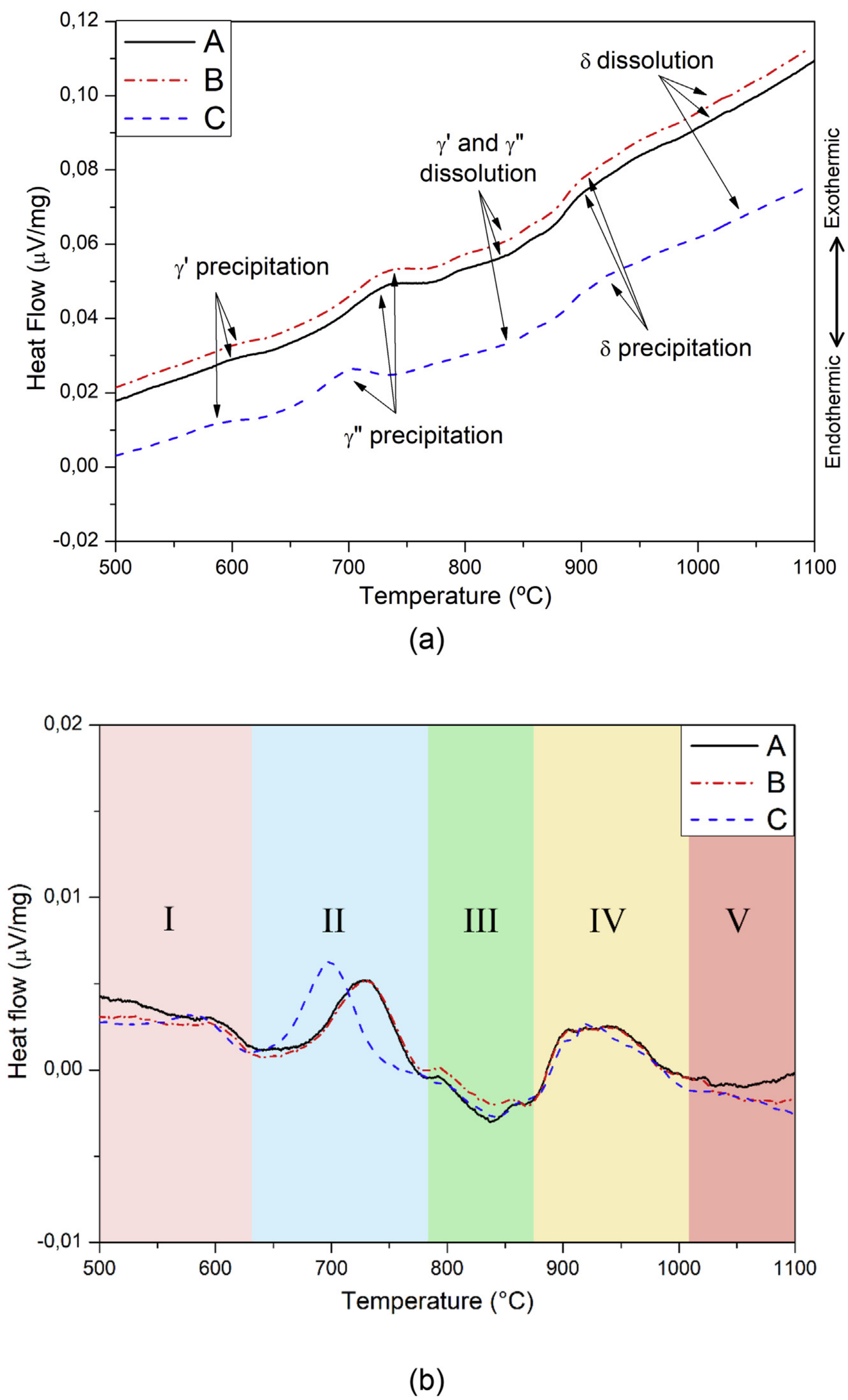

Fig. 6 – DSC curves during heating (a) and DSC normalized curves by subtracting the baseline heat flow (b) of alloys A, B and C. (I) γ′ precipitation; (II) γ" precipitation; (III) γ′ and γ" dissolution; (IV) δ precipitation; (V) δ dissolution and partial melting.

Table 3 – Mean and standard deviation values of the Rockwell C hardness for the samples.

Sample	A	B	C
Hardness (HRC)	37.2 ± 0.3	37.4 ± 1.0	39.3 ± 0.9

The austenitic grain sizes of samples A and C were smaller and the δ area fractions were higher, while sample B showed a bigger austenitic grain size and a smaller δ area fraction. The influence on the grain size would come both from solute drag and Zenner drag, affecting the grain boundary mobility [43], but the relevance of each would vary from sample to sample. Regarding the Zenner drag imposed from the second phase particles, for all samples, initially, its effect would come from the (Ni,Ti) (C,N) strings formed during forging and from the breakage of the primary (Ni,Ti) (C,N) particles. Particularly for Y-alloyed samples B and C, an additional effect would come from the $Ni_{17}Y_2$ phases precipitated, although this effect would be sharply different between B and C samples due to the sharp difference in the quantity and size of the precipitates. However, as the δ phase gradually precipitates along the grain boundaries, the pinning effect increases and grain growth is hindered. But for sample B, as the amount of δ evidenced is lower than for samples A and C, this effect is less relevant. For the solute drag effect, the yttrium influence on the cleanliness of the alloy, especially on oxygen and sulfur, might influence grain boundary segregation and, therefore, grain boundary mobility. As a result, sample B would congregate the conditions for improved mobility of the grain boundaries, with mild influences both from Zenner and solute drags, resulting in a larger grain size. In this way, the Y addition contributes indirectly to δ precipitation due to its controlling effect on mean grain size, which is associated with the grain boundary area and acts as diffusion paths and sites for δ phase nucleation [44]. Consequently, the higher grain boundary area favored the δ precipitation on alloy C and the lower grain boundary area reduced the δ precipitation on alloy B.

3.3. *Thermal analysis*

Fig. 6(a) shows the original DSC curves for the heating cycle of the alloys A, B and C. As the alloys are in the solutionized condition, the precipitation of γ' and γ'' is expected during heating on DSC analysis. The first peaks are observed around 580 °C for alloys A, B and C and are attributed to the γ' phase precipitation. In the range between 640 and 780 °C, noticeable exothermic peaks are evidenced and regarded as γ'' precipitation. However, for alloy C, the peak is shifted to a lower temperature (~700 °C) compared to alloys A and B (~740 °C). The third set of exothermic peaks, around 900 °C for all cases, is regarded to the transformation of γ'' to δ phase and/or the direct precipitation of δ phase from the matrix. These findings are consistent with the work of Niang et al. [45], which addressed the transformations in alloy 718 via DSC. Despite being not mentioned by the above-mentioned study of Niang et al. [45], endothermic peaks were evidenced between the second and third sets of peaks and attributed to the γ' and γ'' dissolution [46,47]. Above around 1000 °C, both Y-added alloys presented a different behavior from the reference alloy, as shown in Fig. 6(b). Besides the dissolution of the δ phase (~1040 °C), the thermodynamic calculations indicated, for the Y-added alloys, a partial melting. Based on the work of Mattern et al. [42], which assessed the Ni-Nb-Y system, although the projection of the liquidus surface would be higher for the compositions adopted in this work, regions of local Y segregation would lead to lower liquidus temperatures. Fig. 6(b) presents the adjusted DSC curves by subtracting the baseline heat flow. This methodology permits a more precise identification of the initiation and end of the transformations.

The A, B and C curves showed similar behaviors. However, the γ'' peak of curve C was significantly shifted to lower temperatures. Since the γ'' precipitation is a nucleation, growth and coarsening process, its kinetics is chiefly controlled by the availability of nucleation sites and the diffusion rate of Nb atoms [48]. The confluence of refined grain size and a higher fraction of secondary phases, like $Ni_{17}Y_2$, would favor nucleation, which can be further improved by the fragmentation and dispersion of the secondary phases, as observed in Fig. 3. In addition, the Y addition would favor the refinement of the dendritic structure [49], smoothing compositional gradients along with the matrix. This is corroborated by the work of Cao et al. [39], who pointed out that Y suppresses the diffusion of carbide-forming elements to the liquid, like Nb. This results in this element being more distributed and available for the precipitation of the γ'' particles.

3.4. *Hardness measurement*

Table 3 presents the Rockwell C hardness measurements for the aged A, B and C alloys. Sample C has a superior hardness when compared to samples A and B. This improved hardness would be supported by the earlier precipitation of the γ'', which is the main hardening phase. A previous initiation of precipitation would result in higher fraction and size of the particles. It is important to note that aging heat treatment, plus the heating rate and time of the test are insufficient to reach a peak hardness. Furthermore, as previously indicated in [15], both the smaller grain size and the higher amount of $Ni_{17}Y_2$ particles have only a secondary role in the hardening process of the alloy, as γ'' is the dominant hardening phase of the alloy.

4. Conclusions

The influence of the yttrium addition on the microstructure of the alloy 718 was studied. Based on the results and discussion presented in this work, it can be concluded:

- For the Y-added alloys, in addition to the usual phases present in the alloy 718, the $Ni_{17}Y_2$ phase was evidenced. Two conditions were identified: 1) associated with the (Nb,Ti) (C,N) and; 2) as isolated particles. For the alloy B, these isolated particles occurred preferentially along grain boundaries, while for alloy C, both inter and intragranular precipitation was evidenced;
- The thermodynamic calculations indicated important segregation of Y and Nb into the liquid during solidification, substantiating the formation of the associated

Nb-rich and Y-rich phases, evidenced for the Y-alloyed samples;

- Alloys A and C presented smaller austenitic grain sizes compared to alloy B. This could be related to the improved grain boundary mobility of alloy B, where a mild Y addition would promote improved cleanliness of the grain boundaries, therefore reducing the solute drag effect but not inducing massive precipitation of $Ni_{17}Y_2$ particles that could promote a relevant Zenner pinning effect, which is considered for alloy C. As a ramification of this effect, the δ phase precipitation was more prominent in alloys A and C, preferentially along grain boundaries, resulting in a higher fraction of δ for these alloys and further hindering grain growth;
- The peaks observed in the DSC curves were related to the γ', γ'' and δ precipitation and dissolution. For γ' and δ phases, no relevant differences between peaks position and width were given. However, for γ'', alloy C presented a curve shifted to lower initiation and peak temperatures. This resulted in more prominent precipitation that impacted strength, as corroborated by the superior hardness of the aged sample.

Declaration of Competing Interest

The authors declare that they have no known competing financial interests or personal relationships that could have appeared to influence the work reported in this paper.

Acknowledgments

The authors would like to acknowledge CAPES, CNPq and FAPERJ for the financial support and Villares Metals for fabricating the material used in this study.

REFERENCES

[1] Reed Rc. The superalloys: fundamentals and applications. 2006.
[2] Donachie MJ, Donachie SJ. Superalloys: a technical guide. 2nd ed. 2002.
[3] Beaubois V, Huez J, Coste S, Brucelle O, Lacaze J. Mater Sci Technol 2004;20:1019–26.
[4] Sundararaman M, Mukhopadhyay P, Banerjee S. Metall Trans A 1988;19:453–65.
[5] Slama C, Servant C, Cizeron G. J Mater Res 1997;12:2298–316.
[6] Di Xu K, Ren ZM, Li CJ. Rare Met 2014;33:111–26.
[7] Amano T. J Rare Earths 2010;28:12–21.
[8] Sun WR, Guo SR, Lee JH, Park NK, Yoo YS, Choe SJ, et al. Mater Sci Eng A 1998;247:173–9.
[9] Jedlinski J, Godlewski K, Mrowec S. Mater Sci Eng A 1989;120–121:539–43.
[10] Zhou PJ, Yu JJ, Sun XF, Guan HR, Hu ZQ. Scripta Mater 2007;57:643–6.
[11] Chen L, Ma X, Wang L, Ye X. Mater Des 2011;32:2206–12.
[12] Li XL, He SM, Zhou XT, Zou Y, Li ZJ, Li AG, et al. Mater Char 2014;95:171–9.
[13] Nunes FC, de Almeida LH, Dille J, Delplancke JL, Le May I. Mater Char 2007;58:132–42.
[14] Nunes FC, Dille J, Delplancke JL, De Almeida LH. Scripta Mater 2006;54:1553–6.
[15] Guimarães AV, Silveira RMS, de Almeida LH, Araujo LS, Farina AB, Dille JAF. Mater Sci Eng A 2020;776.
[16] Li X, He S, Zhou X, Huai P, Li Z, Li A, et al. J Nucl Mater 2015;464:342–5.
[17] Xiao C, Han Y. Mater Sci Eng A 2002;323:58–61.
[18] ling Li Q, rui Zhang H, Gao M, peng Li J, xiao Tao T, Zhang H. Int J Miner Metall Mater 2018;25:696–703.
[19] Zhou PJ, Yu JJ, Sun XF, Guan HR, Hu ZQ. Trans Nonferrous Met Soc China (English Ed.) 2012;22:1594–8.
[20] Deen KM, Afzal N, Ahmad R, Niazi Z, Ayub R, Farooq A, et al. Surf Coating Technol 2012;212:61–6.
[21] Pang HT, Edmonds IM, Jones CN, Stone HJ, Rae CMF. Superalloys 2012;2012:301–10.
[22] Wufeng D, Tietao Z, Heli L, Shangping L, Peiying L. Rare Met Mater Eng 2008;37:1549–54.
[23] Ping YU, Wen W, Fuhui W. J Rare Earths 2011;29:119–23.
[24] Wang W, Yu P, Wang F, Zhu S. Surf Coating Technol 2007;201:7425–31.
[25] Amano T, Isobe H, Sakai N, Shishido T. J Alloys Compd 2002;344:394–400.
[26] Kang DS, Koizumi Y, Yamanaka K, Aoyagi K, Bian H, Chiba A. Mater Lett 2018;227:40–3.
[27] Aimone PR, Mccormick RL. Superalloys 1992;1992:817–23.
[28] Stott FH, Wood GC, Fountain JG. Oxid Metals 1980;14:135–46.
[29] Auger MA, De Castro V, Leguey T, Tarcísio-Costa J, Monge MA, Muñoz A, et al. J Nucl Mater 2014;455:600–4.
[30] Sun D, Liang C, Shang J, Yin J, Song Y, Li W, et al. Appl Surf Sci 2016;385:587–96.
[31] Heilmaier M, Reppich B. Metall Mater Trans A Phys Metall Mater Sci 1996;27:3861–70.
[32] Nardone VC, Tien JK. Scrita Metall 1986;20:797–802.
[33] Cai D, Zhang W, Nie P, Liu W, Yao M. Mater Char 2007;58:220–5.
[34] Andersson J-O, Helander T, Höglund L, Shi P, Sundman B. Calphad 2002;26:273–312.
[35] TCNI8, TCS Ni-based superalloys database, version 8.0. 2022. Accessed March, 5.
[36] TCOX6, TCS met. Oxide solut. Database. 2022. Accessed March, 5.
[37] A. International. ASTM E112-13 - standard test methods for determining average grain size. 2013. West Conshohocken, PA.
[38] Wang Y, Ran R, xiang Zhang Y, Fang F, song Wang H, kun Xia Y, et al. Mater Sci Eng A 2021;823:141726.
[39] Cao S, Yang Y, Chen B, Liu K, Ma Y, Ding L, et al. J Mater Sci Technol 2021;86:260–70.
[40] Kawazoe Y, Landolt H, Otfried M. Numerical data and functional relationships in science and technology. 22nd ed. Berlin: Landolt-Bornstein; 2016.
[41] Zhou YX, Hu MY, Yan P, Shi X, Chong XY, Feng J. RSC Adv 2018;8:41575–86.
[42] Mattern N, Zinkevich M, Löser W, Behr G, Acker J. J Phase Equilibria Diffus 2008;29:141–55.
[43] Hu GW, Zeng LC, Du H, Wang Q, Fan ZT, Liu XW. Intermetallics 2021;136.
[44] Dahotre NB, Mccay MH, Mccay TD, Hubbard CR, Porter WD, Cavin OB. Scripta Metall Mater 1993;28:1359–64.
[45] Niang A, Viguier B, Lacaze J. Mater Char 2010;61:525–34.
[46] Hasani N, Dharmendra C, Sanjari M, Fazeli F, Amirkhiz BS, Pirgazi H, et al. Mater. Characterifile 2021;181:111499.
[47] Calandri M, Yin S, Aldwell B, Calignano F, Lupoi R, Ugues D. Materials (Basel) 2019;12.
[48] Mei Y, Liu Y, Liu C, Li C, Yu L, Guo Q, et al. J Alloys Compd 2015;649:949–60.
[49] dong Bian W, rui Zhang H, Gao M, ling Li Q, peng Li J, xiang Tao T, et al. Vacuum 2018;152:57–64.